

Vacancies making jerky flow in complex alloys

Zhida Liang*^{1,6}, Fengxian Liu², Li Wang³, Zihan You⁴, Fanqi Zhong⁴, Alan Cocks⁵, Florian Pyczak¹

1. Institute of Materials Research, Helmholtz-Zentrum hereon GmbH, Geesthacht, Germany
2. Faculty of Engineering, University of Twente, Enschede, Netherlands
3. State Key Laboratory of Powder Metallurgy, Central South University, Changsha, China
4. School of Metallurgy and Environment, Central South University, Changsha, China
5. Department of Engineering Science, University of Oxford, Oxford, UK
6. Department of Materials Science and Metallurgy, University of Cambridge, Cambridge, UK

*Corresponding author.

E-Mail addresses: zhida.liang@outlook.com (Z. Liang)

Abstract

Longevity of materials, especially alloys, is crucial for enhancing the sustainability and efficiency of various applications, including gas turbines. Jerky flow, also known as dynamic strain aging effect, can indeed have a significant impact on the fatigue life of high-temperature components in gas turbines¹. In general, three jerky flow types, *i.e.*, A, B and C, existed in superalloys². Type A and B, occurring at low temperature, were proved to be caused by interstitial elements, *such as* carbon³. However, Type C serration at high temperature has not been verified directly and remains unresolved, which was unanimously agreed it is caused by the interaction between solute elements and dislocations². In this study, our new discovery challenged this mainstream axiom. We proposed that vacancies play a dominant role in inducing jerky flow instead of solute atoms. By transmission electron microscopy, we observed directly that dislocations are pinned by vacancy-type dislocation loops (PDLs) or dipoles. Our findings suggest that vacancies located at dislocation jogs are primarily responsible for pinning and unpinning of superlattice dislocations. As dislocations move and interact with vacancies, PDLs or dipoles are left behind in their path. This pinning and unpinning process is repeated as successive dislocations encounter the newly formed PDLs or dipoles, leading to the recurring fluctuations in the stress, *i.e.*, serrated flow. Additionally, antisite defects created by Co, Cr and Ti sitting on Ni positions is postulated to facilitate vacancy formation and migration towards dislocations via nearest neighbor jumps. This study provides a new avenue to show how future alloy design can improve the fatigue life of superalloys in extreme environments.

Main

Dynamic strain aging (DSA) or jerky flow during plastic deformation was discovered in the last century and has been observed in a wide range of materials, particularly Mg alloys⁴, Al alloys⁵, high entropy alloys⁶, Ni-based superalloys^{8,9} etc.¹⁰, and in various states. The stress-strain instability is not only observed in crystalline materials but also in amorphous alloys^{11,12}. Microstructural observations indicate that jerky flow is often accompanied by Lüders bands¹², dynamic strain aging^{13,14} or precipitates shearing¹⁵. Banerjee *et. al.*¹⁶ classified jerky flow in plastic deformation into the two broad types: **i.** local strain softening and a sudden stress drop during precipitates shearing; **ii.** dynamic interactions between dislocations and diffusing solute atoms, DSA. This kind of flow instability in a deforming alloy strongly depends on the specific conditions, such as the presence of solute atoms, strain rate and temperature.

There is a consensus that the underlying mechanism for jerky flow at low temperatures is associated with interstitial carbon atoms, while at higher temperatures, there is divergence of opinion as to which element is responsible for DSA⁸. In superalloys with a high content of Mo and Cr, such as Inconel 617¹⁷, Superni 263¹⁸, Alloy-625¹⁹, SPONS10²⁰, Alloy 617M²¹, it was pointed out that the substitutional elements Mo or Cr are responsible for Type C serration at high temperature. However, this hypothesis has not yet been directly verified.

In this research, we present direct evidence and provide a novel explanation for the Type C jerky behavior observed in γ' -phase hardened superalloys, a phenomenon not previously documented. Our findings unveil a direct correlation between vacancies and the manifestation of jerky flow in a complex composition CoNiCr-based superalloy, incorporating elements such as Cr, Ni, Mo, Co, Al, Ti, and W. This discovery challenges the conventional perspective on Dynamic Strain Aging (DSA) in such alloys. The distinct jerky flow behavior predominantly occurs within the temperature range of 400 - 850 °C in the current superalloy. Our investigation delves into the relationship between Type C jerky flow and substitutional elements using advanced techniques such as atomic resolution analytical transmission electron microscopy (STEM) and atomic resolution analytical energy dispersive X-ray spectroscopy (EDS). To gain further insights, molecular simulations were systematically conducted to

examine the formation energy of narrow dislocation dipoles and dislocation loops. To illustrate the intricate process of dislocation pinning and depinning, we employed a three-dimensional discrete dislocation dynamics (3D-DDD) method. This approach considers dislocation glide and vacancy diffusion-assisted self-climb within a unified framework. By integrating these methodologies, our study seeks to advance the comprehension of Type C jerky behavior in superalloys, offering valuable insights for materials science and engineering applications.

Mechanical testing and electron microscopy characterization of dislocation glide and pinning

To demonstrate the effect of the jerky flow mechanism, we chose a novel CoNiCr-based superalloy, which contains the main elements Co, Ni and Cr and other substitutional elements, *i.e.* Al, Ti, Mo and W, see **Extended Data Fig. 1** and **Table 1**. The minor addition of B was added in order to strengthen the grain boundaries and achieve uniform material deformation. The results of compression tests at various strain rates ($\dot{\epsilon} = 10^{-3}$, 10^{-4} and 10^{-5} s⁻¹) and temperatures ($400\text{ }^{\circ}\text{C} \leq T \leq 850\text{ }^{\circ}\text{C}$) are presented in **Fig. 1a** and **Extended Data Fig. 2**. It is obvious, that, if jerky flow is present, the type is the same for all strain rates and temperatures, *specifically*, Type C. According to the characteristics of jerky flow in the entire range of temperatures, the stress initially drops accompanied by a sudden strain change and followed by an increase of stress until the next serration appears. In addition, the magnitude of jerky flow ($\Delta\sigma_{\text{avg}}$) varies with the strain rate and temperature, with the highest magnitude appearing at 600 °C. At relative low temperatures, such as 400 °C, serrations with a very small magnitude were observed at low strain rates (10^{-4} s⁻¹ and 10^{-5} s⁻¹) but disappear when the strain rate is higher (10^{-3} s⁻¹). This indicates that the jerky flow behavior is highly dependent on temperature and strain rate.

After mechanical testing, electron-channeling contrast imaging (ECCI) was employed to identify slip bands along the slipping planes, see **Fig. 1b**, which shows a high density of shearing bands acting as heterogeneous nucleation sites for accommodating moving dislocations. In order to accurately identify dislocation pinning and unpinning along shear bands, the dislocation shearing behavior in the γ' phase was investigated directly by MAADF-

STEM imaging, see **Fig. 1c**. This image shows a dislocation that has glided along the shear direction in the γ' phase being blocked by some defects, which were subsequently identified as PDLs or dipoles.

Nanoscale or sub-nanoscale PDLs are formed by agglomerations of self-interstitial atoms or vacancies on a habit plane which can occur through various processes, such as quenching²², plastic deformation²³ and irradiation damage²⁴. In order to determine the nature of the dislocation loops, the Burgers vector of the loops is first examined. The invisibility criterion ($\vec{g} \cdot \vec{b} = 0$) was employed to determine the Burgers vector \vec{b}_A of the blocked dislocation and the Burgers vectors \vec{b}_1 and \vec{b}_2 of the dislocation loops, see **Fig. 1d**, **Extended Data Fig. 3** and **Table 2**. The Burgers vector of the blocked dislocation is determined to be $\vec{b}_A = \pm a/2 [110]$. This is also the most probable result for the two dislocation loops “1” and “2” in **Fig. 1d**. The line direction of dislocation “A” is close to the $[200]$ crystal direction, **Fig. 1d**, indicating that dislocation “A” is a mixed dislocation with both edge and screw characteristics. In order to accurately determine the Burgers vectors of the dislocation loops, to determine the nature of the loops, the inside-outside contrast method²⁶ was used to determine the $\pm \vec{g}$ diffraction vectors, as depicted in **Extended Data Fig. 4**. Based on the inside-outside contrast analysis, the dislocation loops “1” and “2” were identified as vacancy type PDLs.

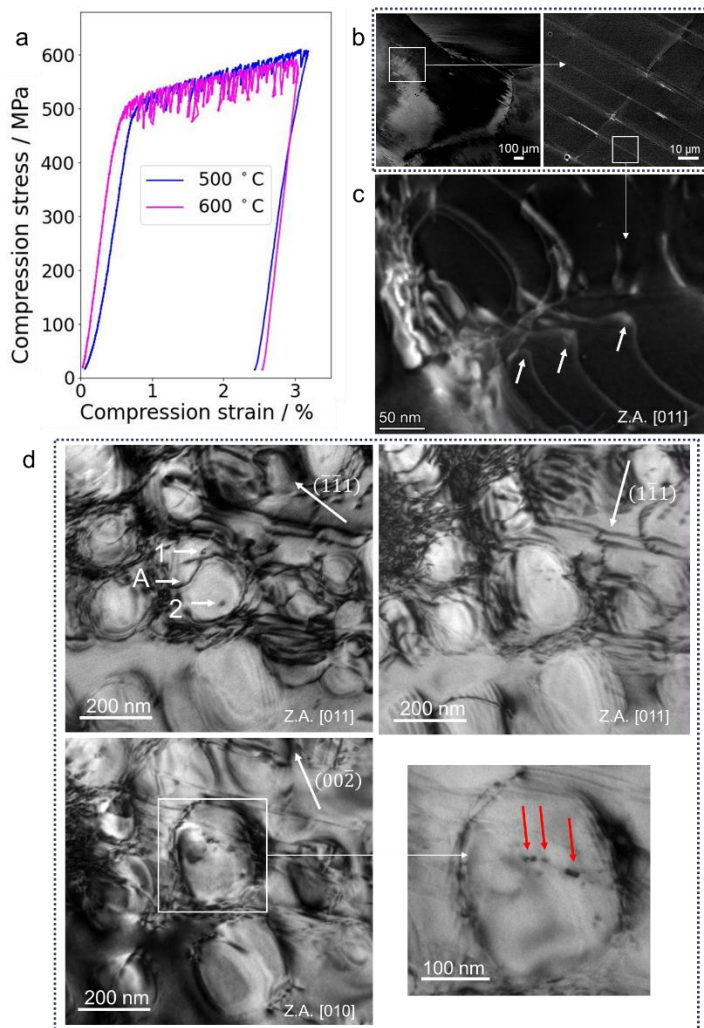


Fig.1. Jerky flow and deformed microstructure. **a.** Stress-strain curves with different temperatures (500-600 °C). **b.** ECCI micrograph showing shearing bands for 3 % strained CoNi-2Mo1W at 600 °C with strain rate of 10^{-4} s^{-1} . **c.** MAADF-STEM image micrograph showing dislocation pinning corresponding to the shearing bands in **b.** **d.** TEM diffraction analysis showing different two-beam conditions in bright field (BF) and the red arrows point out the strange defects behind the shearing dislocation.

Atomic scale characterization of defects

In conventional viewpoint for jerky flow, there should be segregation at defects, *e.g.*, stacking faults or dislocations. In order to prove this, atomic resolution STEM investigation of the specimen deformed at 600 °C was performed. An atomic resolution HAADF-STEM (**Fig. 2a**) image along the [011] zone axis is captured which provides good contrast regarding superlattice intrinsic stacking faults (SISF) and the leading dislocation in the γ' phase. Corresponding COS analysis shows the lattice displacement with deformation gives rise to a high degree of lattice distortion, as demonstrated in **Fig. 2b**. A Burgers circuit was constructed

using the Finish-Start/Right-hand (perfect crystal) (FS/RH) convention, which shows that the projected Burgers vector of the leading dislocation is $\vec{b}_p = a/12 [2\bar{1}1]$. The real Burgers vector should then be $\vec{b}_p = a/12 [2\bar{1}1] + k[011]$, where the multiplier k must be chosen such that the vector \vec{b} represents the total Burgers vector compatible with the fcc lattice. The only possible values are $k = \pm a/4$, for which \vec{b} becomes $a/6 [\bar{1}\bar{2}1]$ and $a/6 [112]$. For further detailed analysis, we carried out atomic-resolution STEM EDS chemical mapping around a Shockley partial dislocation and SISF. **Fig. 2c, d** show atomic resolution STEM-EDS results, respectively, which indicate that there are no substitutional elements (Co, Ni, Cr, Al, Ti, Mo, W) agglomerated around the dislocation core and SF, thus there is chemical homogeneity around the dislocation core without apparent clustering. However, **Extended Data Fig. 5** displays clear segregation around the dislocation core at 750 °C.

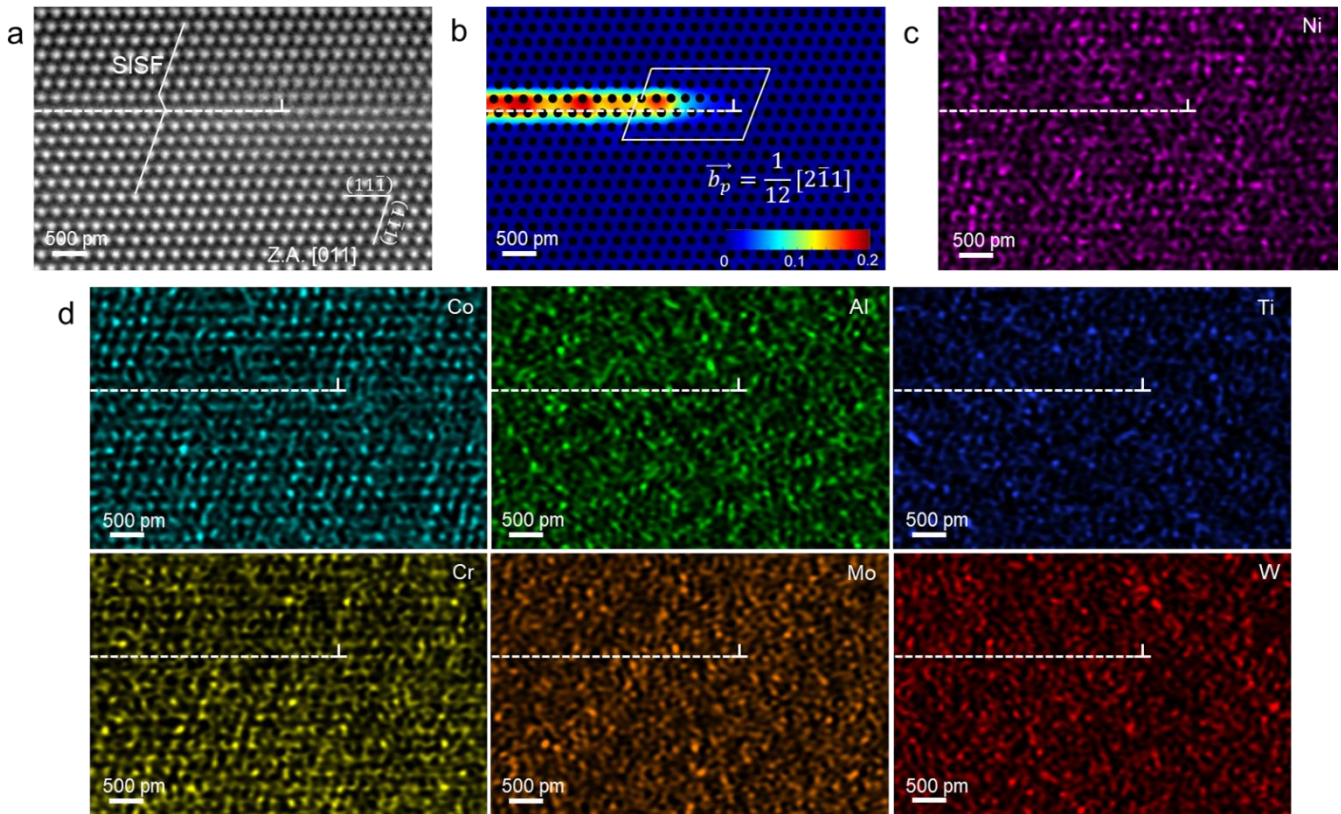


Fig. 2. High resolution STEM-EDS composition maps around a Shockley partial dislocation core. a STEM HAADF image with a [011] zone axis showing a Shockley partial dislocation (indicated by symbol \perp) coexisting with its superlattice intrinsic stacking faults (SISF) (indicated by a dashed line). **b** Corresponding COS analysis revealing exact positions of the partial dislocations related to the SF (Burgers circuit shows the

projected Burgers vector is $\vec{b}_p = a_0/12 [2\bar{1}1]$. **c, d** EDS composition map of Co, Ni, Cr, Al, Ti, Mo and W around the dislocation core showing a homogeneous distribution with random fluctuation but without enrichment or clustering of any specific element.

According to the results demonstrated above, there is substitutional element segregation at faults and dislocations in γ' precipitates, but only when the deformation temperature is above 700 °C. However, the Type C jerky flow mainly happens between 400 and 600 °C. Therefore, in the present alloy, the Type C jerky flow behavior might have no relationship with substitutional element diffusion. In the literature, the chemical diffusivities of Co and Cr (D_{Co} and D_{Cr}) were used for equilibrium phase calculations and kinetics with the Thermo-Calc software (database TTNI8) and DICTRA (database MOBNI3)²⁷. It was found that during plastic deformation at low temperatures ($T < 700$ °C), the diffusion processes are limited and the dislocations need to cut into the γ' -precipitates without the assistance of segregation²⁷. This conclusion aligns with the observations in the present case that there is no segregation at 600 °C but there is at 750 °C. Based on this, we conclude that element clustering is not responsible for Type C serrations in the present superalloy. At least, there is no segregation phenomena in the samples tested at 600 °C.

Dislocation loops and dipoles in the γ' phase

In order to reveal more structural information about the unknown defects or dislocation loops, the region of interest including the dislocation dipole and loops was investigated along the [011] beam direction by HRTEM. By conventional TEM in **Fig. 3a**, the region of interest was targeted in diffraction vector $\vec{g} = 200$, which shows a high density defects left in the γ' precipitate after dislocation shearing. HRTEM was used in order to further confirm the Burgers vectors of the dislocation loop and dipole, see **Fig. 3b**. This method provides only the projection of the Burgers vector in the plane of the TEM foil, *i.e.* (011) plane. After taking high resolution images, the images were processed by Fourier filtering. In **Fig. 3c**, the projected Burgers vector ($\vec{b}_p = a/4 [21\bar{1}]$) of the dislocation was determined precisely by a Burgers circuit defined by Finish-Start/Right-hand (perfect crystal) (FS/RH) convention,

where a is the lattice constant. This is consistent with a Burgers vector of either $a/2 [110]$ or $a/2 [10\bar{1}]$. Both of these Burgers vectors are possible and align with the most highly stressed slip systems of type $a/2 \langle 110 \rangle (11\bar{1})$. In addition, absence of an extra plane of atoms within a crystalline structure was confirmed directly by inverse FFT imaging, see **Fig. 3d**, which confirms that the dislocation loop was avacancy type PDL.

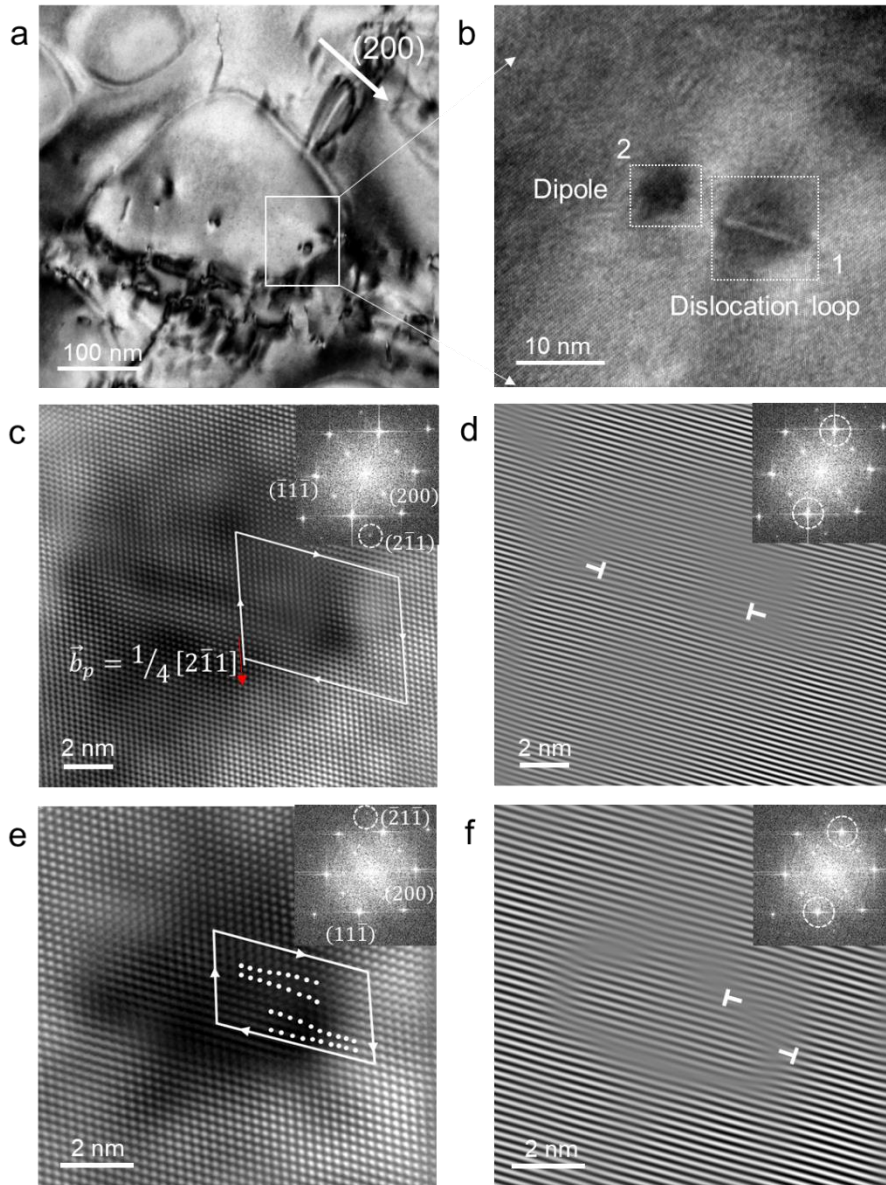


Fig. 3. Conventional TEM observation of dislocation dipoles and dislocation loops. **a** Conventional TEM image in diffraction vector $\vec{g} = 200$ ($s_g = 0$) and closing $[011]$ beam direction (the inset is a magnified image for dislocation loop “1” and dipole “2”). **b** HRTEM image for dislocation loop “1” and dipole “2”. **c, d** iFFT images for vacancy type dislocation loops “1” in the $[011]$ beam direction (the inset is the related FFT

pattern). **e, f** IFFT images for vacancy type dislocation dipole “2” in the [011] beam direction (the inset is the related FFT pattern).

On the other hand, a high resolution image, along the [011] direction, shows a small dislocation dipole across its two edge superlattice dislocation arms. The dipoles are almost perpendicularly elongated with respect to the edge super partial dislocation Burgers vector, $\vec{b} = \pm a/2 [110]$ or $\pm a/2 [10\bar{1}]$. The (111) slip planes of the edge dislocations are separated by a few atomic spacings, indicating the vacancy character of the dipole. Molecular dynamic simulations in **Extended Data Fig. 6**, utilizing the three embedded-atom method for the interatomic potentials, have shown that the formation energies for all the stable interstitial configurations in 30° faulted dipoles of Ni₃Al structure are two to three times those of vacancies. Our calculation confirms that the energetically favorable formation of vacancy-type PDL outweighs that of interstitial-type, providing an explanation for the observed prevalence of vacancy type dipoles and loops.

3D-DDD modeling: the role of vacancy-type dislocation loops and dipoles

A 3D-DDD model is employed to examine the interactions between dislocations, loops and vacancies. Jogs are usually formed as a result of interactions between dislocations and vacancies or PDLs. Depending on their characteristics and height, these jogs exert different pinning effects on the parent dislocations: Jogs on edge dislocations, in general, are able to follow the parent dislocations by glide, although experiencing a higher Peierls stress, as they are restricted to move on non-closely packed slip planes. Jogs on screw dislocations, however, can only climb along the slip direction of their parent dislocations, resulting in a stronger dragging effect. Different drag mechanisms are, therefore, proposed based on jog height. Small jogs typically move along the screw parent dislocations by absorbing/emitting vacancies, this is referred to as the jog dragging mechanism^{28,29}. As the jog height increases, a higher stress is required to drag the jog. Instead of jog dragging, two edge arms along the slip direction form around the pinned jog, which subsequently pinch off by climb to release the parent dislocation while leaving behind an elongated edge dipole; this is known as the dipole dragging mechanism^{28,29}. This elongated edge dipole then breaks off to form a string of PDLs to

decrease the total dislocation energy. For even taller jogs, their climb motion requires extensive matter diffusion, favorable only at high temperatures and under high stresses, resulting in strong pinning of the parent dislocation.

We examine here, employing 3D-DDD simulations, different jog dragging mechanisms, to illustrate the dislocation pinning and unpinning processes. A unified 3D-DDD model^{30,31}, that jointly considers dislocation glide and climb motions, is adopted. The initial configuration is a jogged-screw dislocation with Burgers vector along the $[\bar{1}01]/2$ direction, as shown in **Fig.4a**. The shaded plane represents one of the effective $\langle 111 \rangle$ ‘slip planes’ in the FCC crystals. Edge jogs with heights of 5 nm (jog A), 30 nm (jog B) and 15 nm (jog C) were examined under compressive loading along the $[001]$ direction. Other parameters used here are listed in the **Extended data Table 4**.

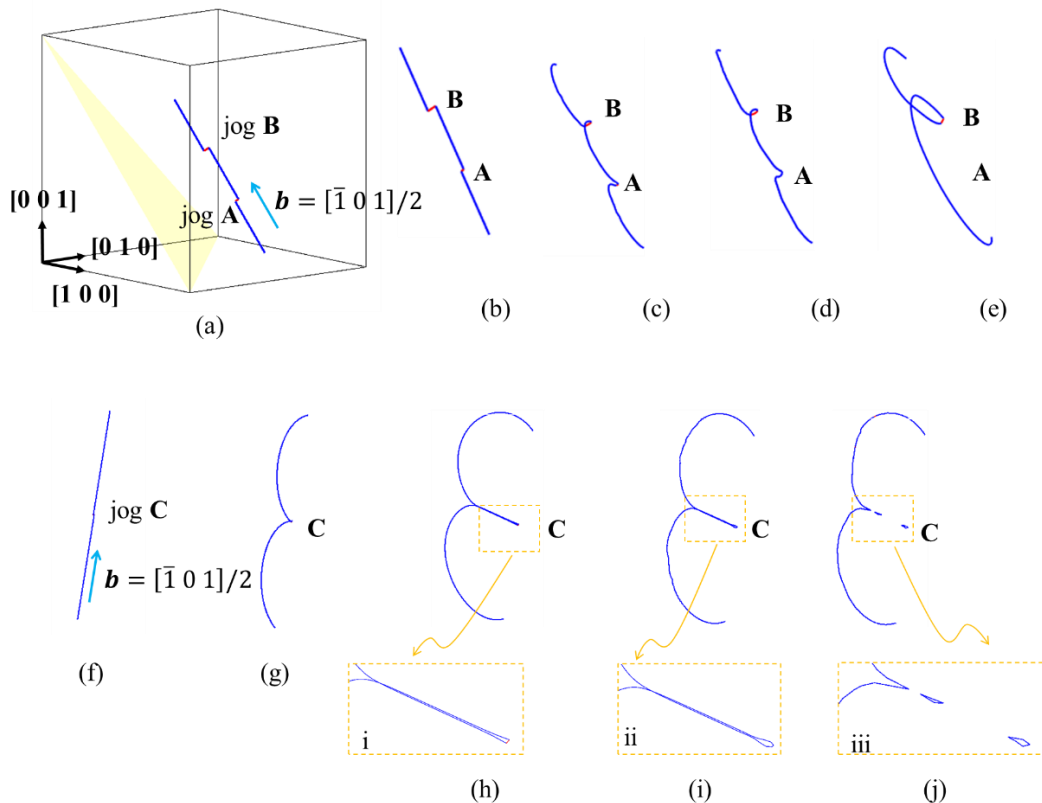


Fig. 4. 3D-DDD simulations of coupled glide and climb motions, showcasing the pinning and unpinning process of a jogged screw dislocation. **a** The simulation box with an initial dislocation configuration consisting of two jogs (highlighted in red, labeled as A and B) with respective heights of 5 nm and 30 nm.

The shaded plane indicates the $\langle 111 \rangle$ slip plane. **b-e** Snapshots depicting the evolution of dislocation configurations under compressive stress along the $[001]$ direction which matches the configuration captured by the TEM images provided in **Extended Data Fig. 7**. Jog **A** is dragged to climb with the parent screw dislocation, eventually disappearing and providing a temporary dragging effect to the parent dislocation. In contrast, the larger jog **B** remains immobile, serving as a robust pinning point, leading to the formation of a Frank-Read source. **f** An initial configuration of a screw dislocation containing a jog labeled as **C**, measuring 15 nm in height. **g, h** Snapshots show dislocation configurations as the screw dislocation bows out. With the screw Frank-Read source bowing out, two parallel edge arms form around the immobile jog **C**, resulting in the formation of an open-ended edge trapping dipole. **i, j** PDLs formed by the two arms sequentially pinching-off from the end of the edge dipole by self-climb to relief the high local curvature.

Snapshots of the dislocation profiles during the evolution are illustrated in **Fig. 4**, where the largest jog, **i.e.** jog **B**, remains immobile, serving as a robust pinning point to the parent dislocation, while the smallest jog, jog **A**, is dragged to move along the parent dislocation through climb by absorbing (antistite-) vacancies, and is eventually destroyed, offering only a limited pinning effect. The lack of a recurring effect on the motion of subsequent dislocations rules out their potential contribution to serrated flow. Jog **C**, of medium height, however, not only exhibits a temporary pinning effect on the leading dislocation, but also leaves behind a series of immobile PDLs, which will interact with subsequent dislocations that glide through this region. As illustrated in **Fig. 4. f - j**, as the screw FR source bows out, it forms an elongated open-end edge dipole around jog **C**. The high curvature at the end of the dipole drives the self-climb of dislocations to rearrange the local atoms to relief the line-tension. This leads to the sequential pinch-off of the two edge arms from the end, releasing the parent dislocation while leaving behind a string of PDLs. Furthermore, this recurring formation and destruction of medium-height jogs typically, as a result of repeated interaction with vacancy-type PDLs, occurs within an intermediate temperature range. At lower temperature, self-climb is negligible, breaking off of the elongated edge dipole will then occur over a much longer time scale. While, at high temperatures, the PDLs left by the leading dislocation become more mobile, and exert a weaker pinning effect. This aligns well with the occurrence of serrated flow, demonstrating a potential link between the generation of dipoles and PDLs and the observation of serrated flow.

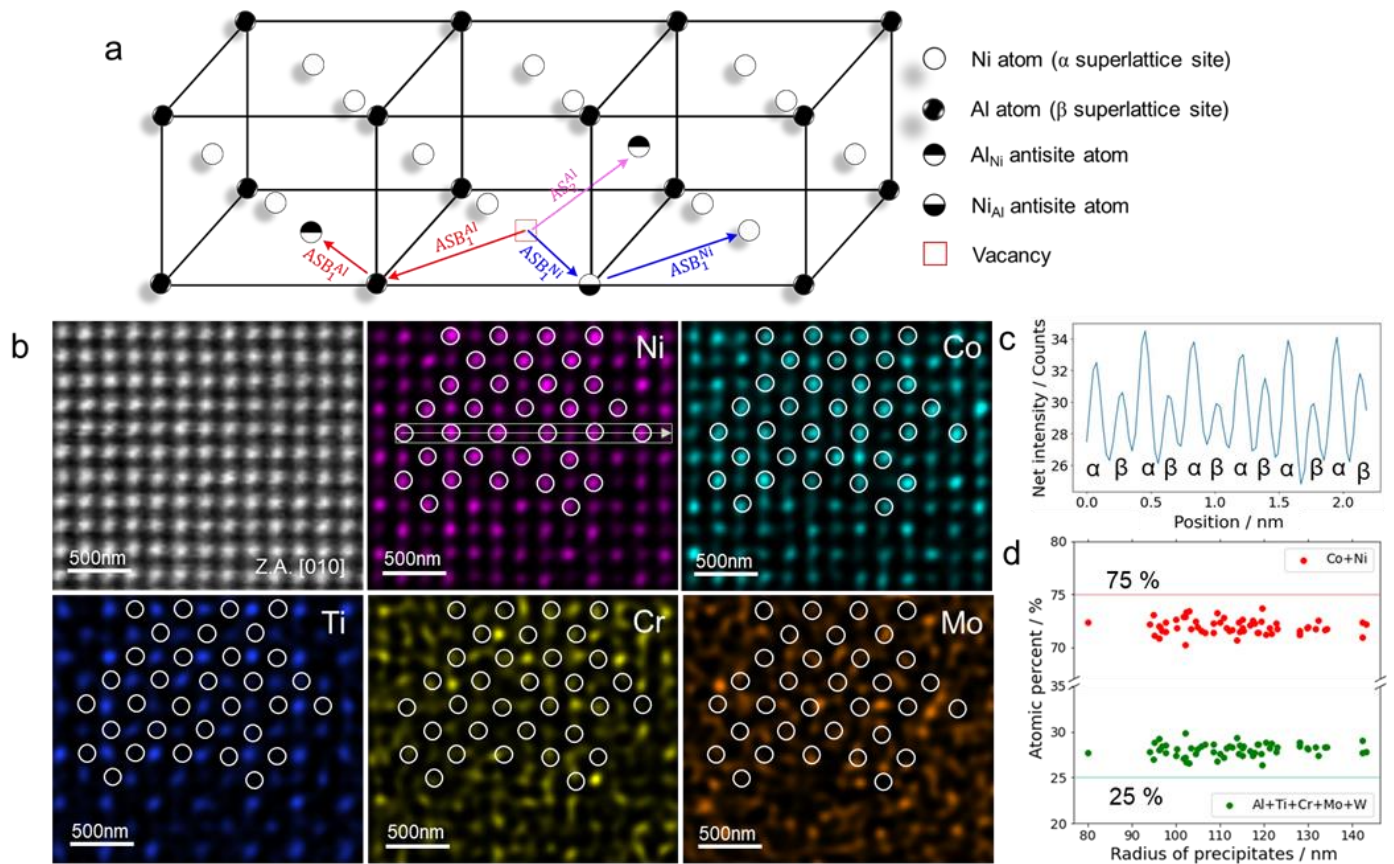


Fig. 5. Vacancy jump paths, atom positions and non-stoichiometric ratio in the γ' phase. **a.** Schematic of vacancy jump paths via the ASB and AS mechanism in Ni_3Al based on reference³². **b.** Quantified atomic resolution EDS elemental maps at atomic scale on a [110] zone axis in the γ' phase. **c.** The composition fluctuation of Ni atomic column in the [010] crystal direction. **d.** The sum of Co+Ni and Cr+Al+Ti+Mo+W concentration in 60 γ' particles, respectively.

Currently, there still is one important question: What kind of driving force drives vacancy diffusion at the intermediate temperature?

Supersaturation of vacancies and anti-site defects in γ' phase

It appears to be possible that vacancy diffusion in ordered phases is supported by the presence of a significant anti-structural disorder at low temperature. This “anti-structural bridge” (ASB)³², as a substructure or percolating cluster, requires not only vacancies but also pre-existing anti-site defects. An elementary bridge event involves one vacancy and one anti-site defect, and consists of two nearest-neighbor (NN) jumps of the vacancy. Anti-site defects exist in Ni_3Al γ' phase, *i.e.* some Co/Ni atoms occupying the β sub-lattice site or Ti/Al

occupying the α sub-lattice site. Gopal et. al.³³ calculated three different anti-site assisted jump pathways for the atoms Ni, Al and vacancy exchange by first-principles, along the pathways shown in **Fig. 5a**. The first one is a vacancy on an α sub-lattice site V_{Ni} first exchanges with a Ni anti-site defect Ni_{Al} and then with a regular atom on the Ni sub-lattice, *i.e.* ASB_1^{Ni} . The second one is a vacancy on the α sub-lattice switches positions with an Al atom on the β sub-lattice, and then with an Al anti-site (Al_{Ni}), *i.e.* ASB_1^{Al} . The third one is vacancy which can also diffuse via the antistructure (AS) sub-lattice mechanism involving simple NN jumps on the α sub-lattice, *i.e.* AS_2^{Al} . Besides, the formation energy of vacancies decreases significantly when Co is substituted at the Ni sublattice which facilitates vacancies to supersaturate in the γ' phase. Cr and Ti will also prefer to exchange with vacancies according to activation energy calculations by the AS_2^{Al} pathway. Therefore, high contents of Co, Cr, Ti in the γ' phase will assist jump exchanges between vacancies and anti-sites in the α sub-lattice (Ni sitting position). **Extended data Table 3** lists several possibilities for vacancy or solutes migration barriers. Apparently, the direct exchange between a vacancy in the α sub-lattice or in the β sub-lattice and Al in β sub-lattice has the highest migration barrier energy. Analysis of the migration paths for Al, Cr, Co, and Ti in Ni_3Al reveal that the energy barriers for solutes and vacancies is lower in the antisite assisted (AS) mechanism. By making a comparison with the activation energy for jerky flow in the present alloy determined by the stress drop method (**Extended data Fig. 8**), the exchange of Cr and Ti solutes with vacancies is the most likely process that promotes vacancies to cluster in dislocation jogs to cause jerky flow.

In order to verify antistructure defects indirectly, each atom position was verified by atomic resolution EDS in **Fig. 5b** and **c**. By analyzing Ni atom column composition fluctuation in **Fig. 5c**, we can conclude that Co, Ni sit on α sub-lattice site and Al, Ti, Cr, Mo and W sit on β sub-lattice site. If the Al/Ni molar ratio is not equal to 1/3, the non-stoichiometric ratio in the γ' phase then indicates antisite atoms exist. Therefore, we measured the composition of 60 particles by STEM-EDS to confirm the non-stoichiometric ratio presented in **Fig. 5d** and **Extended data Fig. 9**. The combined Co and Ni concentration on average in the γ' phase of

the present alloy is 71.95 at.% which is below the stoichiometric value of 75 at.%. Thus, anti-site defects are extremely likely to exist.

The results show that jerky flow, Type C, is not caused directly by an interaction between moving dislocations with substitutional element solutes, but with vacancies. Antistructure, as a driving force, facilitates the exchange of solutes and vacancies so that vacancies can diffuse towards a dislocation to form a vacancy cluster, which pins the dislocation and triggers screw segment of the dislocation to cross-slip into a different glide plane. As the applied stress is increased, it becomes easier to generate a dipole. When the applied stress is high enough, the dipole pinches off and vacancy type dislocation loops or dipoles are left behind as the dislocation continues to glide through the material. By activation energy analysis, it is demonstrated that Ti or Cr additions has the highest possibility to trigger jerky flow in high content Co superalloys. Therefore, we have to find an alternative way, such as tuning Co, Ti or Cr alloy additions in superalloys and eliminating antisite defects, to realize good mechanical properties, excellent corrosion resistance and invisible serrated flow in the future.

Acknowledgement

The author Dr. Zhida Liang thanks Prof. Rachel A. Oliver and EPSRC grant (EP/P00945X/1) support for Transmission Electron Microscopy experiments in the Wolfson Electron Microscopy Suite at University of Cambridge.

References

1. S. L. Mannan, (1993). Role of dynamic strain ageing in low cycle fatigue. *Bulletin of Materials Science*, 16, 561-582.
2. K.Gopinath, A.K. Gogia, S.V. Kamat, U. Ramamurty, (2009). Dynamic strain ageing in Ni-base superalloy 720Li. *Acta Materialia*, 57(4), 1243-1253.
3. R.A. Mulford, U.F. Kocks, New observations on the mechanisms of dynamic strain aging and of jerky flow. *Acta Metall.* 27, 1125-1134 (1979).
4. S.M. Zhu, J.F. Nie, (2004). Serrated flow and tensile properties of a Mg-Y-Nd alloy. *Scripta Materialia*, 50(1), 51-55.
5. A.W. Zhu, (1998). Strain localization and formation of heterogeneous distribution of shearable ordered precipitates: application to an Al-10 at.% Li single crystal. *Acta materialia*, 46(9), 3211-3220.
6. D. Utt, S. Lee, Y. Xing, H. Jeong, A. Stukowski, S.H. Oh, K. Albe, (2022). The origin of jerky dislocation motion in high-entropy alloys. *Nature communications*, 13(1), 4777.

7. M. Knapek, J. Pešička, P. Lukáč, P. Minarik, R. Kral, (2019). Peculiar serrated flow during compression of an FeAlCrMo medium-entropy alloy. *Scripta Materialia*, 161, 49-53.
8. C.Y. Cui, Y.F. Gu, Y. Yuan, H. Harada, (2011). Dynamic strain aging in a new Ni-Co base superalloy. *Scripta Materialia*, 64(6), 502-505.
9. K. Gopinath, A. K. Gogia, S.V. Kamat, U. Ramamurty, (2009). Dynamic strain ageing in Ni-base superalloy 720Li. *Acta Materialia*, 57(4), 1243-1253.
10. U. Fröbel, F. Appel, (2002). Strain ageing in γ (TiAl)-based titanium aluminides due to antisite atoms. *Acta materialia*, 50(14), 3693-3707.
11. Y.I. Golovin, V.I. Ivolgin, V.A. Khonik, K. Kitagawa, A.I. Tyurin, (2001). Serrated plastic flow during nanoindentation of a bulk metallic glass. *Scripta Materialia*, 45(8), 947-952.
12. F.H. Dalla Torre, D. Klaumünzer, R. Maaß, J.F. Löffler, (2010). Stick-slip behavior of serrated flow during inhomogeneous deformation of bulk metallic glasses. *Acta Materialia*, 58(10), 3742-3750.
13. S.K. Oh, M.E. Kilic, J.B. Seol, J.S. Hong, A. Soon, Y.K. Lee, (2020). The mechanism of dynamic strain aging for type A serrations in tensile flow curves of Fe-18Mn-0.55C (wt.%) twinning-induced plasticity steel. *Acta Materialia*, 188, 366-375.
14. J.H. Nam, S.K. Oh, M.H. Park, Y.K. Lee, (2021). The mechanism of dynamic strain aging for type A serrations in tensile curves of a medium-Mn steel. *Acta Materialia*, 206, 116613.
15. T.S. Rong, (2003). Serrated yielding in the B2-ordered Nb-15Al-20V alloy. *Intermetallics*, 11(2), 151-155.
16. S. Banerjee, U.M. Naik, (1996). Plastic instability in an omega forming Ti-15% Mo alloy. *Acta materialia*, 44(9), 3667-3677.
17. C.V. Rao, N.S. Srinivas, G.V.S. Sastry, V. Singh, (2019). Dynamic strain aging, deformation and fracture behaviour of the nickel base superalloy Inconel 617. *Materials Science and Engineering: A*, 742, 44-60.
18. J. Jadav, K.V. Rajulapati, K.B.S. Rao, N.E. Prasad, (2019). Effects of strain rate and temperature on tensile properties, deformation and dynamic strain ageing behavior of Ni-base superalloy Superni 263. *INAE Letters*, 4(4), 241-250.
19. A. Chatterjee, G. Sharma, R. Tewari, J.K. Chakravarty, (2015). Investigation of the dynamic strain aging and mechanical properties in alloy-625 with different microstructures. *Metallurgical and Materials Transactions A*, 46(3), 1097-1107.
20. A. Chiba, X.G. Li, M.S. Kim, (1999). High work-hardening rate and deformation twinning of Co-Ni-based superalloy at elevated temperatures. *Philosophical Magazine A*, 79(7), 1533-1554.
21. V. Shankar, A. Kumar, K. Mariappan, R. Sandhya, K. Laha, A.K. Bhaduri, N. Narasaiah, (2017). Occurrence of dynamic strain aging in Alloy 617M under low cycle fatigue loading. *International Journal of Fatigue*, 100, 12-20.
22. I. Kovacs, L. Zsoldos, *Dislocations and plastic deformation* Pergamon Press, Oxford (1973).
23. D. Hull, D.J. Bacon, *Introduction to dislocations* (4th ed.), Butterworth-Heinemann, Oxford (2001).
24. G.S. Was, *Fundamentals of radiation materials science metals and alloys*, Springer, Berlin (2007)
25. P. Xiu, H. Bei, Y. Zhang, L. Wang, K.G. Field, (2021). Stem characterization of dislocation loops in irradiated FCC alloys. *Journal of Nuclear Materials*, 544, 152658.

26. M.L. Jenkins, M.A. Kirk, (2000). Characterisation of radiation damage by transmission electron microscopy. CRC Press.
27. D. Barba, T.M. Smith, J. Miao, M.J. Mills, R.C. Reed, (2018). Segregation-assisted plasticity in Ni-based superalloys. *Metallurgical and Materials Transactions A*, 49(9), 4173-4185.
28. Karthikeyan S, Viswanathan G B, Mills M J. Evaluation of the jogged-screw model of creep in equiaxed γ -TiAl: identification of the key substructural parameters[J]. *Acta materialia*, 2004, 52(9): 2577-2589.
29. Li Y, Ghoniem N, Baker K, et al. A coupled vacancy diffusion-dislocation dynamics model for the climb-glide motion of jogged screw dislocations[J]. *Acta materialia*, 2023, 244: 118546.
30. F. Liu, A.C. Cocks, E. Tarleton, (2020). A new method to model dislocation self-climb dominated by core diffusion. *Journal of the Mechanics and Physics of Solids*, 135, 103783.
31. F. Liu, A.C.F. Cocks, E. Tarleton, Dislocation climb driven by lattice diffusion and core diffusion[J]. *Journal of the Mechanics and Physics of Solids*, 2023, 176: 105300.
32. C.R. Kao, Y.A. Chang, (1993). On the composition dependencies of self-diffusion coefficients in B2 intermetallic compounds. *Intermetallics*, 1(4), 237-250.
33. P. Gopal, S.G. Srinivasan, (2012). First-principles study of self-and solute diffusion mechanisms in γ' -Ni₃Al. *Physical Review B*, 86(1), 014112.
34. H. Wang, D. Xu, R. Yang, P. Veyssi re, (2008). The transformation of edge dislocation dipoles in aluminium. *Acta Materialia*, 56(17), 4608-4620.
35. P. Hirel, (2015). AtomsK: A tool for manipulating and converting atomic data files. *Computer Physics Communications*, 197, 212-219.
36. X.W. Zhou, R.A. Johnson, H.N.G. Wadley, (2004). Misfit-energy-increasing dislocations in vapor-deposited CoFe/NiFe multilayers. *Physical Review B*, 69(14), 144113.
37. Y. He, Z. Liu, G. Zhou, H. Wang, C. Bai, D. Rodney, R. Yang, (2018). Dislocation dipole-induced strengthening in intermetallic TiAl. *Scripta Materialia*, 143, 98-102.
38. A.P. Thompson, H.M. Aktulga, R. Berger, D.S. Bolintineanu, W.M. Brown, P.S. Crozier, S.J. Plimpton, (2022). LAMMPS-a flexible simulation tool for particle-based materials modeling at the atomic, meso, and continuum scales. *Computer Physics Communications*, 271, 108171.
39. X.Zhang, H. Deng, S. Xiao, (2014) Diffusion of Co, Ru and Re in Ni-based superalloys: a first-principles study. *Journal of alloys and compounds*, 588, 163-169.
40. F.X. Liu, Z.L. Liu, X.Y. Pei, (2017) Modeling high temperature anneal hardening in Au submicron pillar by developing coupled dislocation glide-climb model. *International Journal of Plasticity*, 99: 102-119.
41. Y. Minamino, S.B. Jung, T. Yamane, K. Hirao, (1992). Diffusion of cobalt, chromium, and titanium in Ni₃Al. *Metallurgical Transactions A*, 23, 2783-2790.

Vacancies making jerky flow in complex alloys

Zhida Liang^{*1,6}, Fengxian Liu², Li Wang³, Zihan You⁴, Fanqi Zhong⁴, Alan Cocks⁵, Florian Pyczak¹

7. Institute of Materials Research, Helmholtz-Zentrum hereon GmbH, Geesthacht, Germany
8. Faculty of Engineering, University of Twente, Enschede, Netherlands
9. State Key Laboratory of Powder Metallurgy, Central South University, Changsha, China
10. School of Metallurgy and Environment, Central South University, Changsha, China
11. Department of Engineering Science, University of Oxford, Oxford, UK
12. Department of Materials Science and Metallurgy, University of Cambridge, Cambridge, UK

*Corresponding author.

E-Mail addresses: zhida.liang@outlook.com (Z. Liang)

Methods

Materials

The alloy under investigation is a γ' -phase hardened polycrystalline CoNiCr-based superalloy named CoNiCr-2Mo1W with the nominal chemical composition Co35Ni15Cr5Al5Ti2Mo1W0.1B (at.%). The actual chemical composition measured by SEM-EDS is listed in **Extended Data Table 1**. The alloy was melted at least 7 times under argon in the form of a 70 g ingot button on a water-cooled copper hearth using a laboratory-scale vacuum arc melting unit. The as-cast material was homogenized at 1250 °C for 24 h, followed by ageing at 900 °C in air for 220 h, and subsequently air cooled to room temperature.

Mechanical testing

Compression tests to determine the 0.2% proof stress of the alloy were performed initially using a strain-controlled closed-loop machine MTS 810 (MTS System Cooperation) operated at various strain rates ($\dot{\epsilon} = 10^{-3}$, 10^{-4} and 10^{-5} s⁻¹) and temperatures ($25 \text{ °C} \leq T \leq 950 \text{ °C}$). Cylindrical compression specimens with a gauge length of 7.5 mm and a diameter of 5 mm were machined from the standard heat-treated material. The sample deformation was monitored by an extensometer attached over a 21 mm gauge length and the extension was used as a feed-back parameter.

Microstructural characterization

The γ/γ' two-phase microstructures of the aged samples were characterized by backscattered electron (BSE) imaging in a scanning electron microscope (FE-SEM, Zeiss, Germany Gemini). After deformation, Electron Channeling Contrast Imaging (ECCI) was performed to investigate slip bands and dislocation structure.

For transmission electron microscopy (TEM) sample preparation, 3 mm disks from the heat-treated samples

were cut and mechanically polished to a thickness of about 75 μm . The final samples were thinned to electron transparency by a twin jet electro polishing unit using the Struers A3 electrolyte with a voltage of 32 V at -38 $^{\circ}\text{C}$. A Thermo Fisher Scientific Talos F200i TEM operated at 200 kV and equipped with a Dual-X Energy Dispersive X-ray Spectroscopy (EDS) detector and the VeloxTM control software was used to investigate composition of the γ' phases of the aged samples and the element distribution along the defects in the γ' phases illustrated in **Extended Data Fig. 6**. In addition, the conventional TEM, FEI Tecnai F20 and Osiris 200, was employed to study defects, *e.g.* dislocations, dipoles and dislocation loops.

The atomic EDS were examined by a double corrected ThermoFisher Scientific Spectra 300 TEM equipped with a four-quadrant Super-X detector. High angle annular dark field (HAADF)-high resolution scanning transmission electron microscopy (HRSTEM) images and atomic resolved EDS maps were recorded at a voltage of 300 kV to determine element distribution and site occupancy in the lattice. The collection angle range of the HAADF detector is 51-200 mrad at a camera length of 145 mm. The collecting parameters for EDS maps and HAADF-HRSTEM images were as follows: convergence angle was 30 mrad ($C_2 = 70 \mu\text{m}$), and probe current was about 50 pA for HAADF-HRSTEM images and around 100 pA for EDS maps. A Radial Wiener filter was applied for the final atomic resolved EDS element maps.

Molecular dynamic simulations

Dipole stability was studied by classical molecular dynamics (MD). Vacancy- and interstitial-type dislocation dipoles in Ni_3Al , with Burgers vectors $\pm 1/2 [110]$, the $4\mathbf{d}$ distance between the two dislocation centers along the $[111]$ direction (\mathbf{d} is the interplanar distance along $[111]$) and orientation angles 90° , 75° , 60° , 45° , 30° and 15° (defined as the angle between the Burgers vector and the line connecting the dislocation centers), were constructed using the methodology developed in Refs.³⁴ and performed on the Atomsk software³⁵. The x, y, z axis of the simulation box was along $ss [1\bar{1}2]$, $[\bar{1}11]$ and $[110]$, respectively, and the size was $14.9 \times 121.9 \times 124.4 \text{ \AA}$ with the periodic boundary condition. An embedded atom interatomic potential for the Ni-Al system³⁶ was employed. The atomic configurations of all kinds of dipoles were relaxed at 1 K for 50 ps and operated at 1000 K for 1 ns with the NVT ensemble and 0.25 fs timestep³⁷, performed on Lammmps software³⁸.

3D-DDD simulations

3D-DDD simulations enable in situ observations of collective dislocation behaviors during plastic deformation and can therefore provide fundamental insights into the mechanisms controlling plastic flow. In this work, we employed the unified dislocation dynamics framework developed by Liu et al.^{30, 31}, which considers both dislocation climb and glide motions. This framework integrates various diffusion mechanisms, including bulk

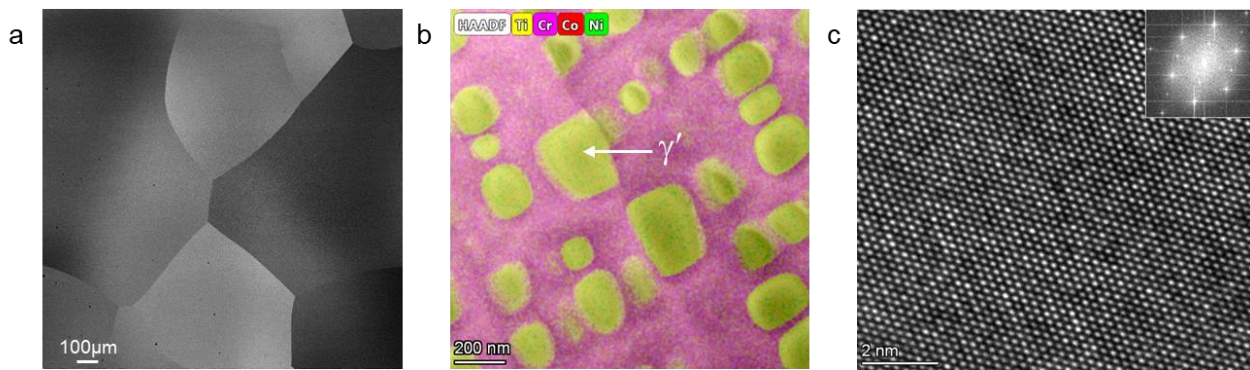
diffusion in the regular lattice and pipe diffusion along dislocation cores, to model dislocation climb. It allows for a comprehensive examination of the interaction among dislocations, vacancies and dislocation loops.

Within this framework, dislocation lines are discretized into sequentially interconnected segments. Each dislocation segment is characterized by a Burgers vector that represents the magnitude and the direction of lattice distortion associated with the segment. The dynamics of each segment is governed by a specific mobility law. Here, a phonon-drag mobility law⁴⁰ for dislocation glide motion in FCC material is adopted. The governing equation for dislocation climb is derived through a variation principle-based approach, coupling both bulk diffusion and pipe diffusion.

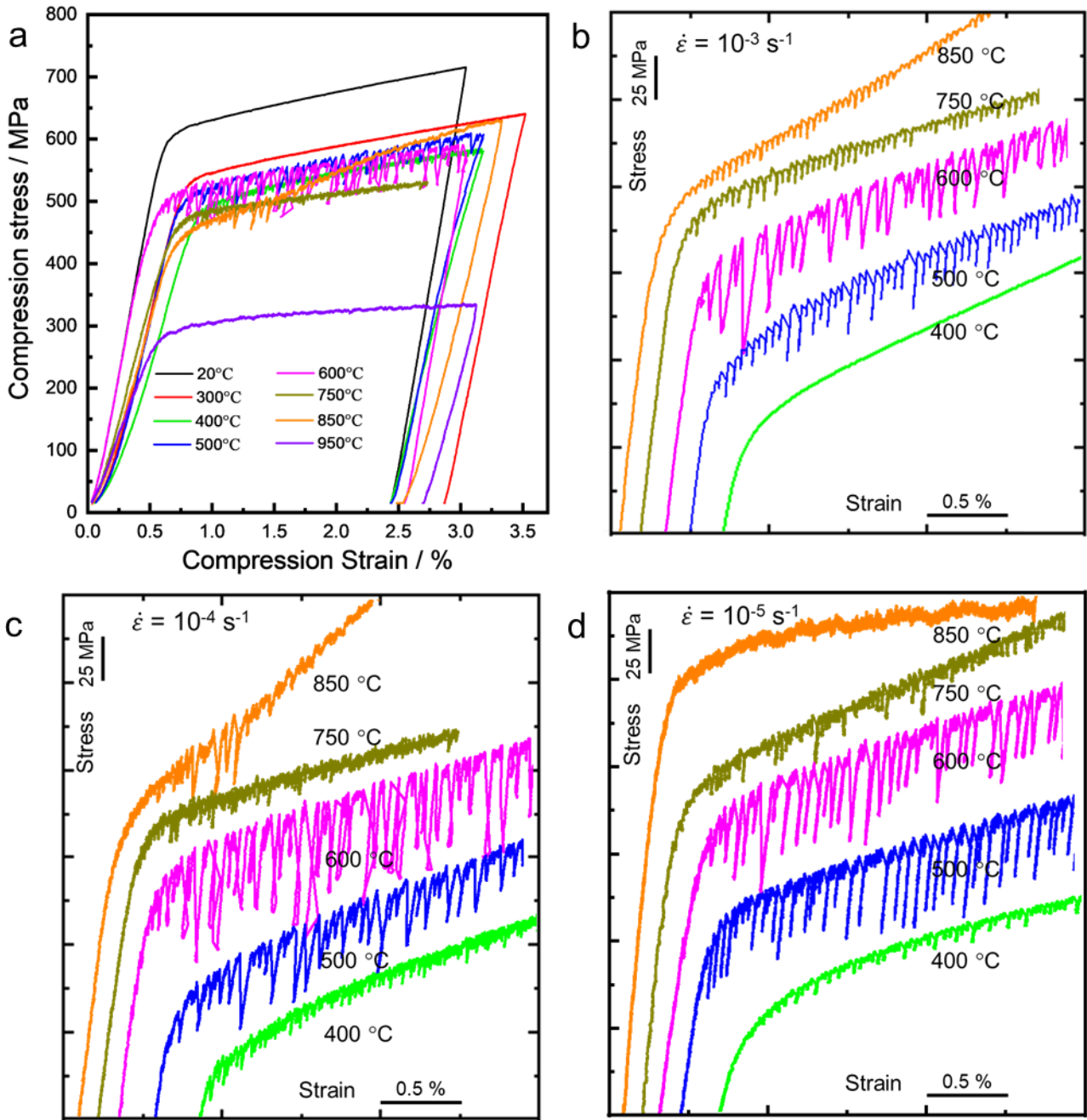
All DDD simulations are conducted on cubic cells with finite boundary conditions, enforced by the finite element method through the superposition principle. The edges of the simulation box were aligned with the three orthogonal crystal directions $X = [100]$, $Y = [010]$, and $Z = [001]$, respectively. The size of the simulation box is $1000b \times 1000b \times 1000b$, where b denotes the magnitude of the Burgers vector. The initial configuration for all simulations consists of screw-type Frank-Read sources with stepped edge jogs of varying heights, and both ends are pinned in place.

Extended Data Table 1. The measured composition (at.%) of the superalloy CoNiCr-2Mo1W by SEM-EDS.

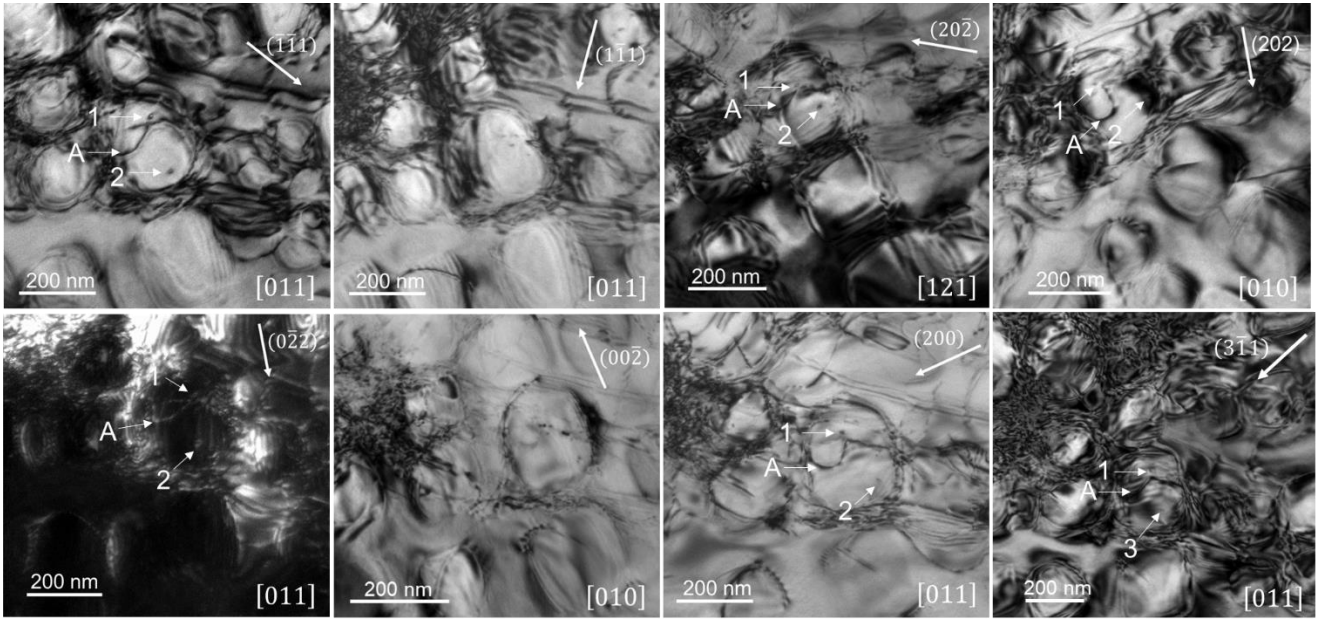
Elements	Co	Ni	Cr	Al	Ti	Mo	W
alloy	37.4	34.3	15.6	4.6	5.3	1.9	0.9



Extended Data Fig. 1. **a.** Back scattering diffraction image of alloy CoNiCr-2Mo1W. **b.** Composite map of the STEM-HAADF image and element distribution (Co, Ni, Cr and Ti). **c.** HRTEM image for specimen.



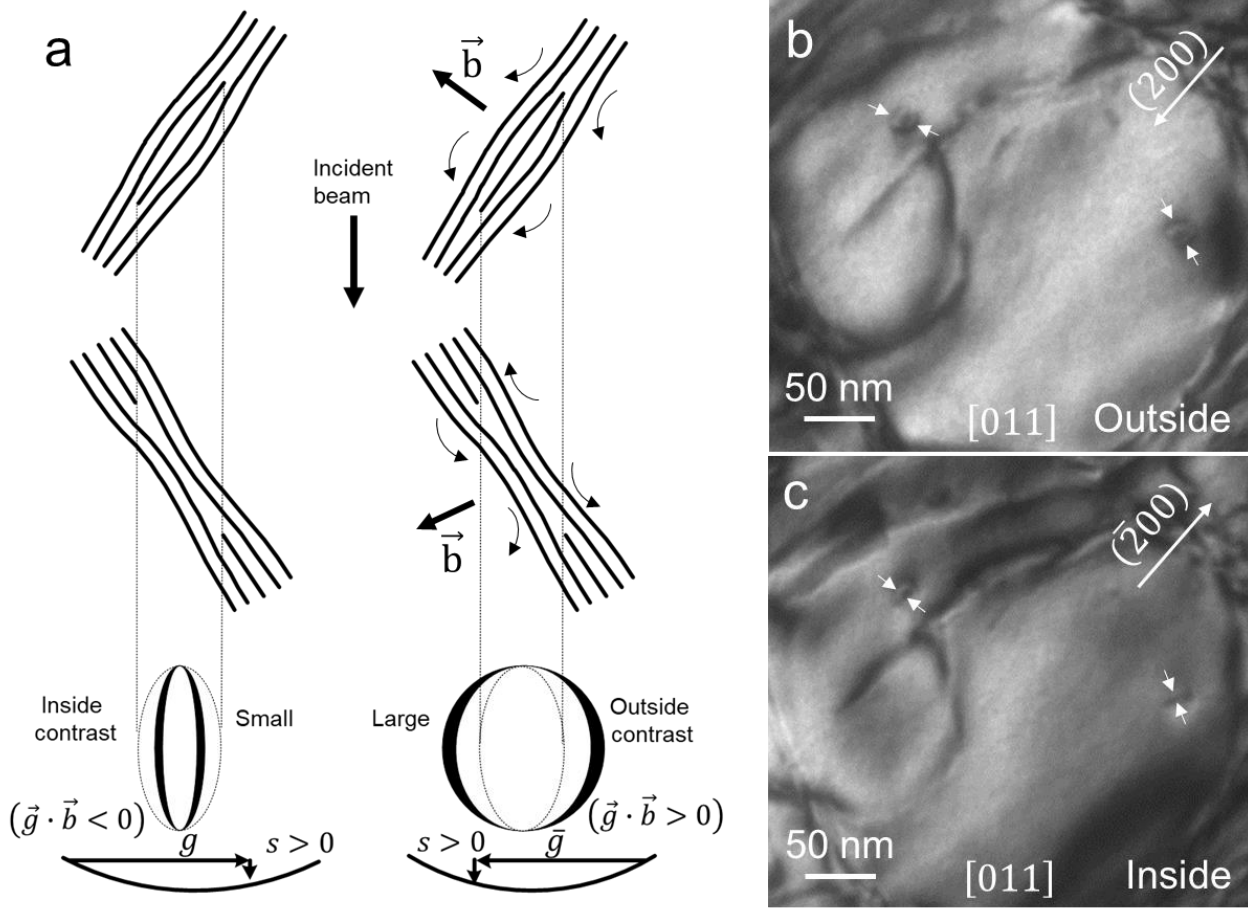
Extended Data Fig. 2. **a.** Typical compression stress-strain curves at different temperatures (from room temperature to 950 °C) at a strain rate of $1 \times 10^{-4} \text{ s}^{-1}$. **b, c, d.** The stress-strain curves with different strain rates ($\dot{\epsilon} = 10^{-3}, 10^{-4}$ and 10^{-5} s^{-1}) and different temperatures (400 - 850 °C).



Extended Data Fig. 3. TEM diffraction analysis ((a)-(c)) showing different two-beam conditions in BF for 3 % strained CoNi-2Mo1W at 600 °C with strain rate 10^{-4} s^{-1} .

Extended Data Table 2. Table of visibility ($\vec{g} \cdot \vec{b}$ series) for dislocations marked in Fig. 3: “+” indicates visible, “w” indicates weak contrast, “-” indicates invisible, “?” indicates no determination possible.

	(200)	($\bar{1}\bar{1}1$)	($0\bar{2}2$)	($1\bar{1}1$)	(202)	($20\bar{2}$)	($00\bar{2}$)	($3\bar{1}1$)	\vec{b}
A	+	+	+	-	+	+	-	+	$\pm \frac{a}{2} [110]$
1	+	+	+	-	w	w	-	w	$\pm \frac{a}{2} [110]$
2	w	+	+	-	w	+	-	w	$\pm \frac{a}{2} [110]$

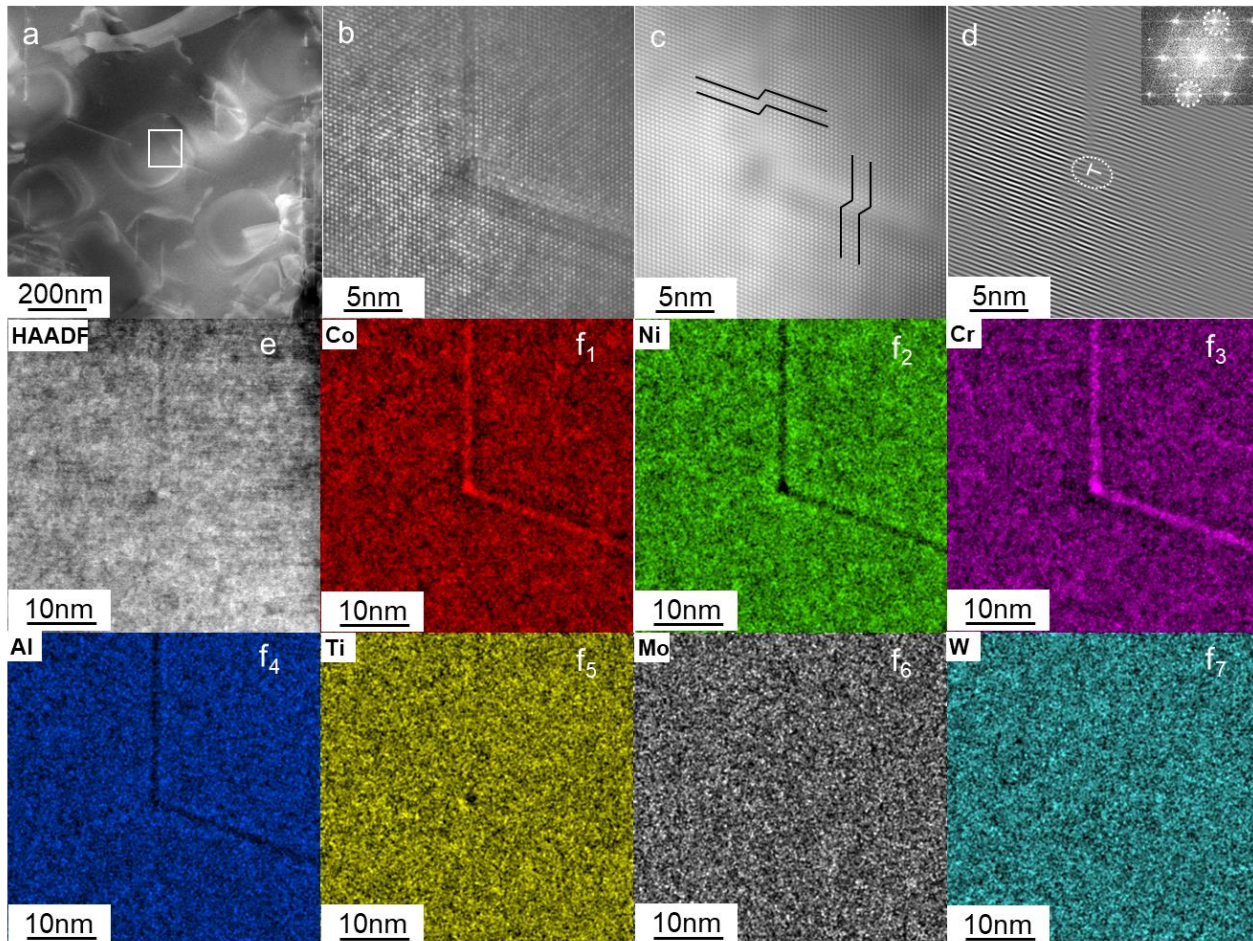


Extended Data Fig. 4. **a** Diagram depicting the “inside” and “outside” contrast condition (deviation error $s_g > 0$) for a vacancy or interstitial dislocation loop. **c, d** show the inside-outside contrast of the dislocation loops in diffraction vectors $\vec{g} = \pm 200$ closing [011] beam direction.

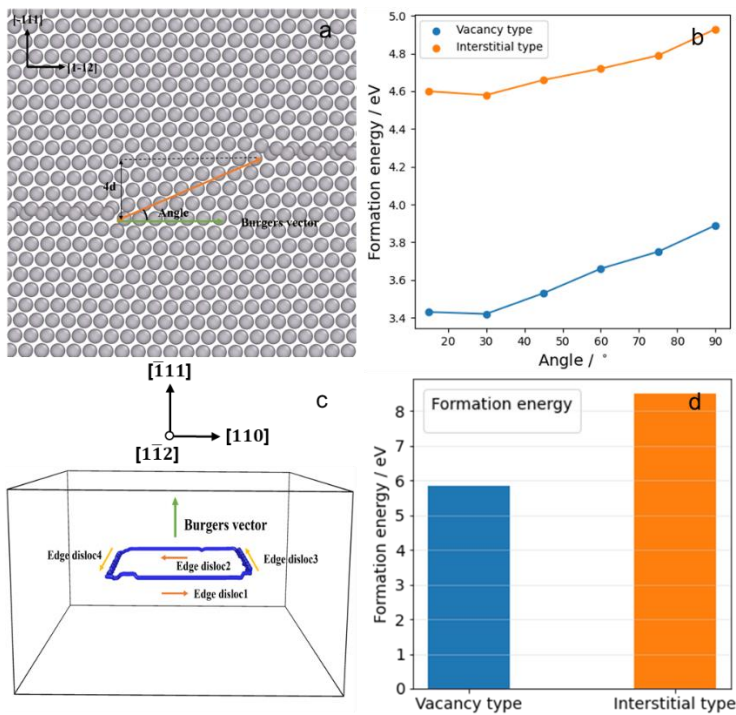
By $\vec{g} \cdot \vec{b}$ series analysis in **Extended Data Table 2**, $\vec{b}_{dl} = \pm a/6 [110]$ is the most possible result for dislocation loops “1” and “2”. In order to further accurately determine the dislocation Burgers vector, the inside-outside contrast method³³ by $\pm \vec{g}$ diffraction vectors was also used to determine the nature of dislocation loops which is depicted schematically in **Extended Data Fig. 4a**. The nature of interstitial and of vacancy dislocation loops, lying on planes inclined to the electron beam, are imaged under bright-field kinematical or dark field weak-beam conditions with $s_g > 0$ using the $\pm \vec{g}$ diffraction vectors shown in **Extended Data Fig. 4a**. Empirically, the inside contrast arises when $(\vec{g} \cdot \vec{b})s_g < 0$, outside when $(\vec{g} \cdot \vec{b})s_g > 0$. Furthermore, the dislocation loops “1” and “2” show outside contrast in diffraction vector $\vec{g} = 200$, inside contrast in diffraction vector $\vec{g} = \bar{2}00$ in **Extended Data Fig. 4b** and **c**, respectively. Therefore, Burgers vectors of dislocation loops “1” and “2” should be $\vec{b}_{dl} = a/6 [110]$. For edge interstitial loops Burgers vector \vec{b} is parallel to the upward-drawn loop normal \vec{n} , *i.e.* $\vec{b} \cdot \vec{n} > 0$ and $\vec{b} \cdot \vec{z} < 0$, where \vec{z} is the beam direction, whilst for edge vacancy loops Burgers vector \vec{b} is antiparallel to \vec{n} , *i.e.* $\vec{b} \cdot \vec{n} < 0$ and $\vec{b} \cdot \vec{z} > 0$. Because of Fig. 9(b)

and (c) being taken in beam direction $\vec{z} = [011]$ with $\vec{b}_{dl} \cdot \vec{z} = 1 > 0$. Therefore, the dislocation loops “1” and “2” are vacancy type dislocation loops. If $\vec{b}_{dl} \cdot \vec{z} < 0$, then the dislocation loop will be an interstitial type dislocation loop.

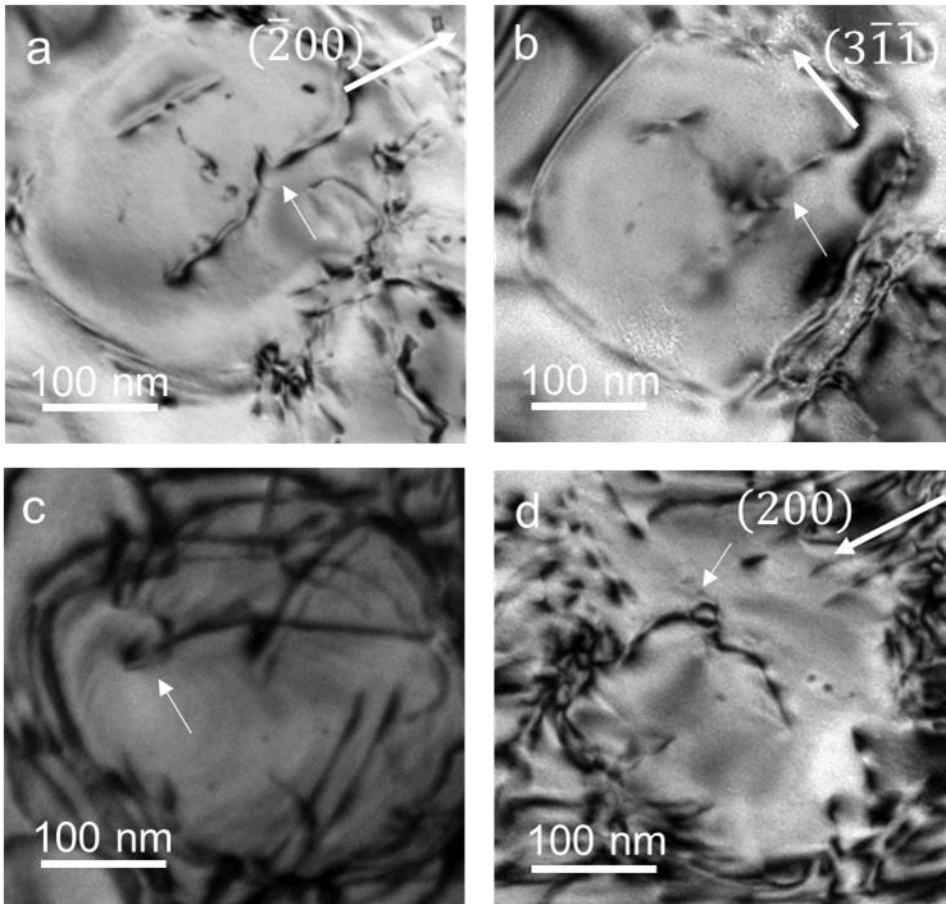
Actually, large-angle convergent-beam electron diffraction (LACBED) is the direct way to deduce both the amplitude and the sign of the Burgers vectors by the intersection “splitting” of the Bragg lines within LACBED patterns with the shadow image of the dislocation lines. It is very difficult to view the shadow image of the dislocation loop with respect to the diffraction pattern in the present cases. Dislocation loops are too small (about 10 nm) so that the “splitting” required for analysis is poor or not visible.



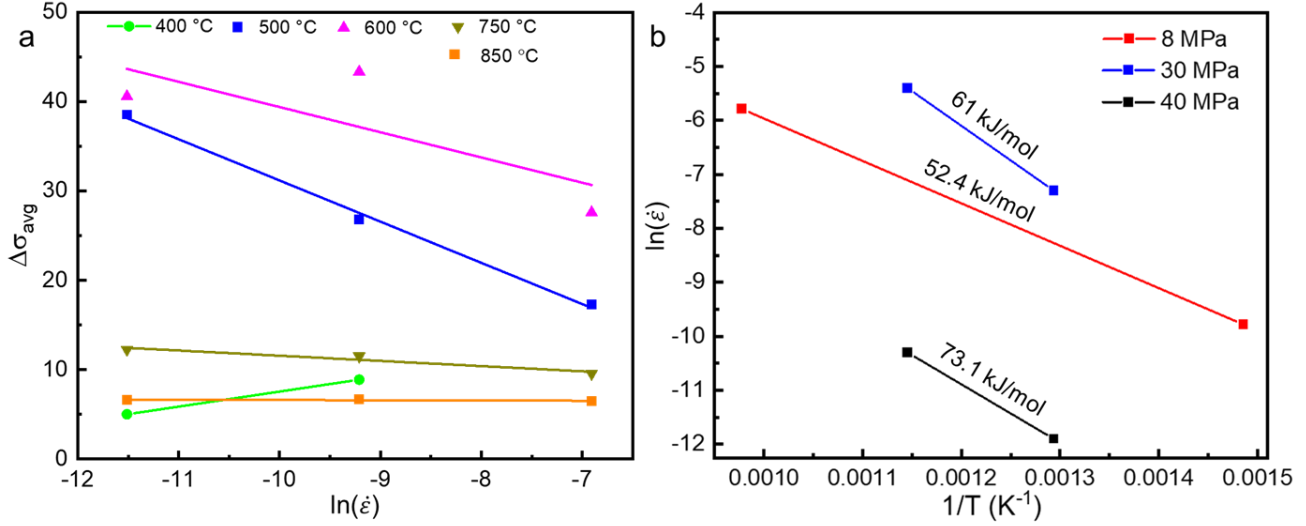
Extended Data Fig. 5. **a** The STEM-MAADF image for dislocation shearing in γ' phase; **b**. Corresponding HRTEM for white rectangle in **Fig. 6a**. **c, d** The related iFFT images for **Fig. 6b**. **e, f** The STEM-HAADF image and elemental maps for the region within the white rectangle in **Fig. 6a**.



Extended Data Fig. 6. **a** Atomic configuration of 60° dipoles with height. **b** Formation energy of vacancy/interstitial type dipoles of various orientations. **c** Schematic configuration of dislocation loop. **d** Formation energy of vacancy/interstitial type dislocation loops.



Extended Data Fig. 7. **a, b** TEM image for jog dragging. **c.** TEM image for dipole bypass. **d.** TEM image for dislocation loop formation. After screw part of dislocation absorbs vacancies, there are four possible scenarios with applied stress variation. **(i.** With super partial dislocation absorbing vacancies, the screw segment part of the dislocation will climb and glide, as the jog drags the dislocation. **ii.** As the jog height increases, the stress required for jog dragging increases significantly and dipole dragging is generated instead. **iii.** When the applied stress is further increase, the two segments of the dislocation start to bypass the jog. **iv.** Then, the two segments pinch-off from each other at cross-slip locations, leading to the formation of a prismatic loop or dipole. The origin of a dislocation loop or dipole is often traceable back to ordinary dislocations, which suggests that it was trailed and terminated at a jogged dislocation.)



Extended Data Fig. 8. a Stress drop $\Delta\sigma_{avg}$ plotted vs. strain rate for different temperatures. **b** Determination of the activation energies (Q) from $\ln(\dot{\epsilon})$ vs $1/T$ plot using intercepts from **a** by the stress drop method.

Stress Drop Method

The activation energy can also be estimated by another method, called the stress drop method⁹. It has been found that the stress drop serves as a better criterion for studying DSA compared to the critical strain method. $\Delta\sigma_{avg}$ is defined as the difference of the stress level for the breakaway of dislocations from their atmosphere and at which they start to glide through the lattice. In the stress-strain curves, $\Delta\sigma_{avg}$ is the height of individual serrations. In this procedure, $\Delta\sigma_{avg}$ at a given strain was calculated for a range of strain rates $\dot{\epsilon}$ and temperatures T . A constant value of $\Delta\sigma_{avg}$ was then selected and the corresponding $\dot{\epsilon}$ was determined for each temperature. Finally, these values of $\dot{\epsilon}$ were plotted as a function of $1/T$ and Q was estimated from its slope as:

$$Q = -(RT \ln \dot{\epsilon}) \quad (1).$$

The Q values for $\Delta\sigma_{avg}$ of 8, 30, 40 MPa are ≈ 52 , 61 and 73 kJ/mol, respectively. The average Q (62 kJ/mol) is similar to Q values in other Ni-based superalloys, such as Wasploy (66 kJ/mol)³² and Inconel-600 (58 kJ/mol)³². In these Ni-based superalloys, Carbon was considered to be responsible for the DSA effects because the activation energy for pipe diffusion of C in Ni is around 69 kJ/mol³³. However, in our alloy no C is present and serrations of Type C are found in all T - $\dot{\epsilon}$ regimes investigated.

Extended Data Table 3. The comparison between calculated migration barriers (kJ/mol) for various solute and vacancy exchanges in Ni₃Al by the first principle study³³ and calculated average activation energy (kJ/mol) for flow serrations by Stress Drop Method. (X_{Ni} indicates element X occupies a Ni site sublattice (β sub-lattice)

position; X_{Al} indicates element X occupies an Al site sublattice (α sub-lattice) position; V_{Al} indicates vacancy occupies an Al site sublattice (α sub-lattice) position; V_{Ni} indicates vacancy occupies a Ni site sublattice (β sub-lattice) position.)

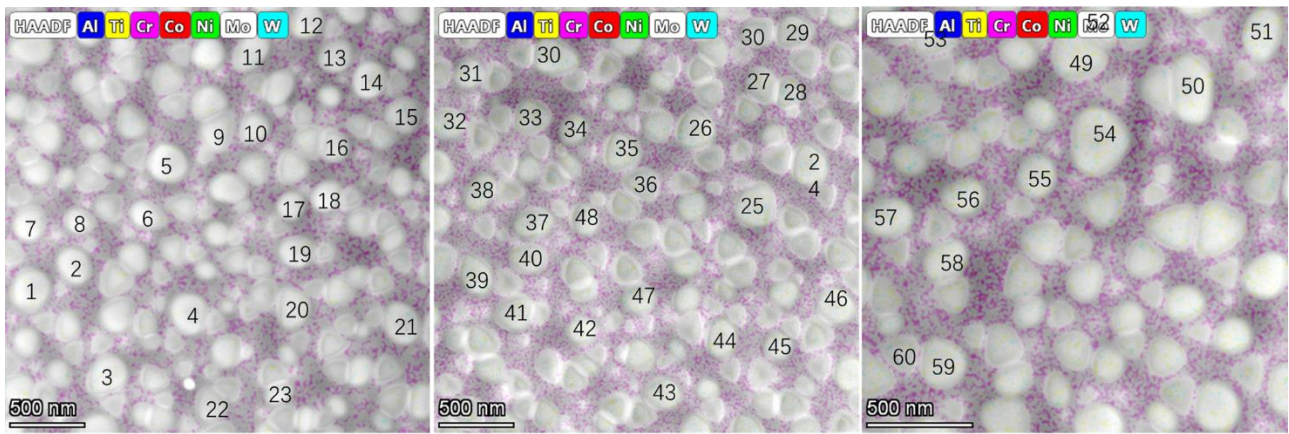
Elements	Ni	Al	Co	Cr	Ti	
$X_{Ni} \rightarrow V_{Ni} (AS_2^X)$	/	77	89	67	28	Stress Drop Method
ASB_1^{Al}	/	82	/	98	77	
ASB_1^{Ni}	91	/	164	/	/	
$X_{Al} \rightarrow V_{Ni}$	/	93	104	164	131	$Q = 62 \pm 10$ kJ/mol
$X_{Al} \rightarrow V_{Al}$	/	324	357	415	338	

In first principle calculation results³³, listed in Extended Data Table 3, the vacancy migration energy is close to activation energy of flow serrations by Stress Drop Method.

In experiment, the activation energies for Co, Cr, and Ti diffusion in the ordered $L1_2$ structured Ni_3Al phase are 325, 366, and 468 kJ/mol, respectively⁴¹.

Extended data Table 4. Parameters adopted in 3D-DDD simulations

Parameters	Magnitude
Shear Modulus	$G = 83$ GPa
Poisson's ratio	$\nu = 0.29$
Burgers vector	$b = 0.2496$ nm
Vacancy migration energy	$U_m^v = 69$ kJ/mol
Vacancy formation energy	$U_f^v = 62$ kJ/mol
Pre-exponential for diffusion	$D_0 = 0.78 \times 10^{-6}$ m ² /s ³⁹



Extended Data Fig. 9. The 60 collected γ' particles for STEM-EDS composition measurement.